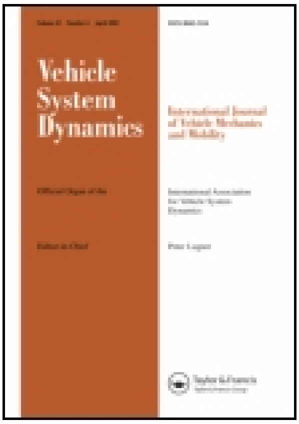

Vehicle System Dynamics: International Journal of Vehicle Mechanics and Mobility

Publication details, including instructions for authors and subscription information:
http://www.tandfonline.com/loi/nvsd20

Development and validation of a wear model for the analysis of the wheel profile evolution in railway vehicles

J. Auciello [a], M. Ignesti [a], M. Malvezzi [b], E. Meli [a] & A. Rindi [a]

[a] Department of Energy Engineering, University of Florence, 50139, Firenze, Italy

[b] Department of Information Engineering, University of Siena, 53100, Siena, Italy

Version of record first published: 13 Jun 2012.

To cite this article: J. Auciello, M. Ignesti, M. Malvezzi, E. Meli & A. Rindi (2012): Development and validation of a wear model for the analysis of the wheel profile evolution in railway vehicles, Vehicle System Dynamics: International Journal of Vehicle Mechanics and Mobility, 50:11, 1707-1734

To link to this article: http://dx.doi.org/10.1080/00423114.2012.695021

Vehicle System Dynamics
Vol. 50, No. 11, November 2012, 1707–1734

Taylor & Francis
Taylor & Francis Group

Development and validation of a wear model for the analysis of the wheel profile evolution in railway vehicles

J. Auciello[a], M. Ignesti[a], M. Malvezzi[b], E. Meli[a]* and A. Rindi[a]

[a]*Department of Energy Engineering, University of Florence, 50139 Firenze, Italy;*
[b]*Department of Information Engineering, University of Siena, 53100 Siena, Italy*

(*Received 23 May 2011; final version received 12 May 2012*)

The numerical wheel wear prediction in railway applications is of great importance for different aspects, such as the safety against vehicle instability and derailment, the planning of wheelset maintenance interventions and the design of an optimal wheel profile from the wear point of view. For these reasons, this paper presents a complete model aimed at the evaluation of the wheel wear and the wheel profile evolution by means of dynamic simulations, organised in two parts which interact with each other mutually: a vehicle's dynamic model and a model for the wear estimation. The first is a 3D multibody model of a railway vehicle implemented in SIMPACK™, a commercial software for the analysis of mechanical systems, where the wheel–rail interaction is entrusted to a C/C++ user routine external to SIMPACK, in which the global contact model is implemented. In this regard, the research on the contact points between the wheel and the rail is based on an innovative algorithm developed by the authors in previous works, while normal and tangential forces in the contact patches are calculated according to Hertz's theory and Kalker's global theory, respectively. Due to the numerical efficiency of the global contact model, the multibody vehicle and the contact model interact directly online during the dynamic simulations.

The second is the wear model, written in the MATLAB® environment, mainly based on an experimental relationship between the frictional power developed at the wheel–rail interface and the amount of material removed by wear. Starting from a few outputs of the multibody simulations (position of contact points, contact forces and rigid creepages), it evaluates the local variables, such as the contact pressures and local creepages, using a local contact model (Kalker's FASTSIM algorithm). These data are then passed to another subsystem which evaluates, by means of the considered experimental relationship, both the material to be removed and its distribution along the wheel profile, obtaining the correspondent worn wheel geometry.

The wheel wear evolution is reproduced by dividing the overall chosen mileage to be simulated in discrete spatial steps: at each step, the dynamic simulations are performed by means of the 3D multibody model keeping the wheel profile constant, while the wheel geometry is updated through the wear model only at the end of the discrete step. Thus, the two parts of the whole model work alternately until the completion of the whole established mileage. Clearly, the choice of an appropriate step length is one of the most important aspects of the procedure and it directly affects the result accuracy and the required computational time to complete the analysis.

The whole model has been validated using experimental data relative to tests performed with the ALn 501 'Minuetto' vehicle in service on the Aosta–Pre Saint Didier track; this work has been carried out thanks to a collaboration with Trenitalia S.p.A and Rete Ferroviaria Italiana, which have provided the necessary technical data and experimental results.

Keywords: railway systems; rail–wheel interaction; wear

*Corresponding author. Email: meli@mapp1.de.unifi.it

ISSN 0042-3114 print/ISSN 1744-5159 online

http://dx.doi.org/10.1080/00423114.2012.695021
http://www.tandfonline.com

1. Introduction

The development of a mathematical model capable of estimating the wheel wear in the railway field is definitely an important aim for safety, economic and logistical reasons. For example, the correct prediction of the wear rate in a particular context may be very important in the planning of the wheelset maintenance interventions. These fundamental operations, which are periodically necessary, are quite onerous both in economic sense and in terms of vehicle availability; hence, it is certainly advantageous to reduce their frequency. In fact, as the wear proceeds to occur, the shape of the wheel profile changes inducing performance variations in the wheelset–rail coupling, especially in the vehicle's guidance and running stability on straight tracks. The development of a contact geometry which may compromise the vehicle stability or increase the derailment risk cannot be allowed and both the phenomena may occur even at relatively low speeds: the hunting is made easier by a high value of the equivalent conicity, while the derailment may be facilitated by low flange contact angles [1,2]. Due to these reasons, the original wheel profile has to be periodically re-established by means of turning; before the end of the life of the wheelset, this processing can be performed only a few times.

As a further application, a reliable wear model can also be used in the optimisation of the wheel profile from the wear point of view. The research on an optimal shape of the wheel for a particular railway application may be useful to guarantee a uniform wear, which implies almost stable characteristics of the contact geometry. In this way, not only the wear rate may be reduced, leading to a higher mean time between two maintenance interventions, but the performance of the wheel–rail contact may also be nearly constant in time.

However, in the development of an accurate wear model [3–5], one of the most critical aspects is the availability of experimental results, since the collection of the data requires at least a few months with relevant economic costs. In fact, besides the general organisational and technical costs, the experimental measurements have to be done on trains which operate in service and periodically their service must be interrupted for data acquisition, with remarkable induced costs. Moreover, the collected data must be opportunely organised to correlate all the main influential factors (vehicle characteristics, tracks, rail conditions, etc.) to the wear evolution. In other words, the route of the vehicle must be exactly known and obviously the measured data must be expressed as a function of the travelled mileage. If online experimental measurements cannot be carried out, the problem can be overcome by deriving experimental proofs on a scaled test rig [3–5].

This paper presents a complete model for the prediction of the evolution of wheel profiles due to wear that involves multibody simulations and a wear model. More precisely, the general layout adopted is made up of two parts that are mutually interactive: the vehicle model (multibody model and wheel–rail global contact model) and a wear model (local contact model, wear evaluation using the above-mentioned experimental law and wheel profile update). The multibody model is implemented with the commercial multibody code SIMPACK™: the accurate 3D dynamic modelling of the vehicle's motion takes into account all the significant degrees of freedom. Starting from the kinematic variable evaluated by the multibody model (wheelset position and orientation and their derivatives), the global contact model, developed by the authors in previous works [6–8], calculates the contact forces between the wheelset and the rail and interacts online with the multibody model to reproduce the vehicle dynamics; in particular, it uses an innovative algorithm for the detection of the contact points between the wheelset and the rail, with a fully 3D semi-analytical approach to the problem. As regards the wear part, the local contact model exploits the outputs of the multibody simulations (contact points, contact forces and global creepages) to calculate the contact pressures and the local creepages inside the contact area, while, thanks to the knowledge of these quantities, the wear model evaluates the amount of removed material and its distribution along the wheel profile; the removal of material and the profile update are carried out considering the fully 3D structure of the phenomenon.

The wheel wear progress is treated as a discrete process by dividing the overall mileage to be simulated in spatial steps: at each step, the dynamic simulations are performed by means of the 3D multibody model keeping the wheel profile constant, while the wheel geometry is updated through the wear model only at the end of the discrete step. The vehicle model and the wear part work alternately exchanging data until the completion of the total mileage. The accuracy of the result and the required computational effort are both strongly affected by the step length, thus its length has to be chosen as a good compromise between these two aspects.

The entire model has been validated by means of the technical and experimental data related to the Aln 501 'Minuetto' vehicle, the measured wear progress provided by Trenitalia S.p.A. as well as the track data given by Rete Ferroviaria Italiana (RFI) and relative to the Aosta–Pre Saint Didier railway line. This is a track with sharp curves of the Italian Railways and the scenario is rather interesting since the Aln 501 'Minuetto' exhibits serious problems on this track in terms of wear, requiring frequent maintenance interventions on the wheels.

2. General architecture of the model

The general layout of the model has been arranged in agreement with Trenitalia S.p.A and RFI, according to the following main working hypotheses:

- discrete approach to the wear evolution, by dividing the entire distance to be simulated in steps and updating the wheel profile after each step;
- the track is not subjected to wear and the rail profiles are always new and kept constant;
- the wheel–rail contact is under dry conditions and
- the wheel profile used in the dynamic simulations is the same for each vehicle's wheel and the output of the wear model is the evolution of a single mean wheel profile to be used in the next step, which includes the effects of the wear on all the wheels of the vehicle.

With respect to the first point, the entire mileage to be simulated is divided into a few spatial steps, in which the wheel profile is maintained constant during the dynamic simulations performed by means of the multibody model; the results of the wear evaluation, at the end of the current step, allow to update the wheel profile for the next step of the procedure. The step length depends on the total distance to be covered and it is one of the most important aspects of the entire numerical procedure, because it directly affects the precision: in fact, the longer the step, the higher the accuracy and the overall computational time; hence the choice has to be a compromise between these aspects. Moreover, from a numerical point of view, the step length can be chosen either constant during the overall distance or variable (introducing, for example, a threshold on the maximum of removed material); nevertheless, the constant step length turns out to be quite a suitable choice for this kind of problem, especially in the case of short distances to be simulated, providing comparable results in terms of accuracy and better performance in terms of numerical efficiency.

Since the wheel wear in railway applications is a phenomenon which requires at least tens of thousands of kilometres (but even hundreds of thousands in most cases) to express its effects, the simulated distances cannot be as long as the real ones to be investigated, because they would require unacceptable computational times, even if the whole track has

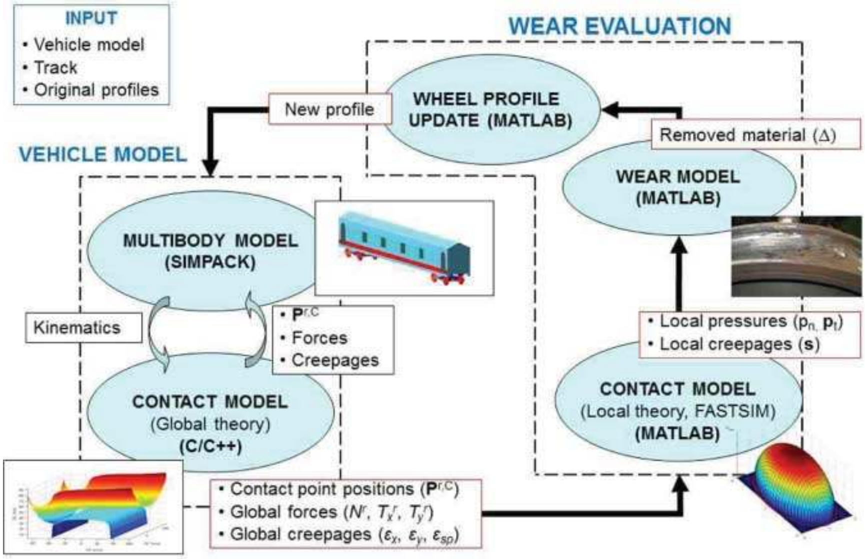

Figure 1. General architecture of the model.

been divided into discrete steps. This issue can be overcome by hypothesising a proportionality between the wear relative to a single discrete step and the amount of wear relative to the distance really simulated by means of the numerical multibody model (i.e. the two wear rates are the same); this hypothesis is reasonable only if the numerically simulated track is a significant representation, in statistical terms, of the track associated with the discrete spatial step.

A diagrammatic representation of the whole model is provided in Figure 1: it includes two main parts that work alternatively during each step. On the left side, there is the *vehicle model*, the part which is responsible for the dynamic simulations, made up of the multibody model and the global contact model; the two subsystems interact online with each other during the simulations to reproduce the vehicle dynamics. On the right side, there is the *wear evaluation*, which comprises three subparts: the local contact model, the wear model and the wheel profile update.

In more detail, during the simulations, in the first task of each procedure step, the multibody model implemented in SIMPACK exchanges data continuously at each time step with the global contact model [6–8], passing the wheelset kinematic variables (wheelset position and orientation and their derivatives) and receiving the positions of the contact points, the wheel–rail contact forces and the global creepages. Once the multibody simulations are completed, the local contact model (written in MATLAB and based on the FASTSIM algorithm [9]) evaluates, starting from the global contact variables ($\mathbf{P}^{\mathrm{r}}_{\mathrm{C}}$, N, T_x, T_y, ϵ_x, ϵ_y and ϵ_{sp}), the contact pressures, the local creepages and, consequently, the total frictional work ($\mathbf{p}_t$, p_n, $\mathbf{s}$, L_F) inside each detected contact patch; the removed material and its distribution along the wheel profile are then obtained passing these data to the wear model, by means of the experimental relationship [3–5]. Finally, the wheel profile is updated through suitable numerical procedures.

The evolution of the wheel wear can be approached in different manners, depending on the goals of the study. If the aim is the analysis of the phenomenon on a long track or on a complex railway line with many vehicles in service, a statistical approach is necessary to achieve generally significant results in a reasonable time. In this work, the entire considered railway track (the Aosta–Pre Saint Didier railway line) has been substituted with an equivalent set of different curved tracks, classified by radius, superelevation and travelling speed, built consulting a detailed track database provided by RFI. Therefore, simulations have not been performed on the real railway line, but they have been carried out on an equivalent representation of this railway net, derived by means of statistical methods.

The presented model architecture allows the achievement of good performance in terms of both accuracy and numerical efficiency; in particular, such performance can be achieved mainly thanks to the following innovative elements: the new global contact model (Section 3.2) developed by the authors, which substantially improves the accuracy of the distribution of the contact points, and the procedure aimed at the profile update due to wear, which will be described in detail in Section 4.3.

3. The vehicle model

3.1. *The multibody model*

The railway vehicle on which this study has been performed is the ALn 501 Minuetto (Figure 2), a passenger transport unit widely used by the Italian Railways. It is made up of three coaches and four bogies with two wheelsets; the external bogies are motorised (Figure 3), whereas the two intermediate trailer bogies are of Jacobs type, shared between two coaches (Figure 4).

Similar to most parts of passenger trains, the bogies are provided with two stages of suspensions. The primary suspensions, which link the axle boxes with the bogie frame, are constituted by Flexicoil springs, made up of two coaxial springs, which mainly provide the vertical stiffness in this stage. Since the stability against the hunting at high speeds in straight tracks requires higher longitudinal and lateral stiffnesses, the first is entrusted to a longitudinal linking arm which connects the axle box with the frame, while the second is provided by a bushing element. A nonlinear damper is responsible for the damping of the vertical relative displacements.

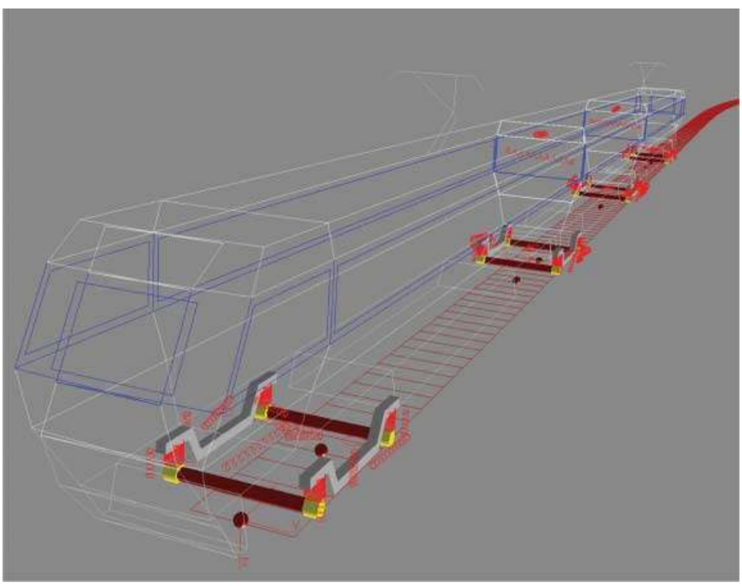

Figure 2. The Aln 501 Minuetto multibody model.

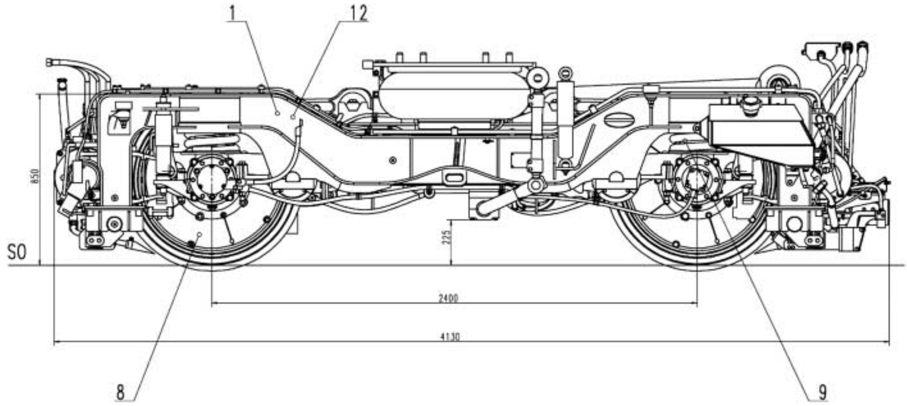

Figure 3. The motor bogie.

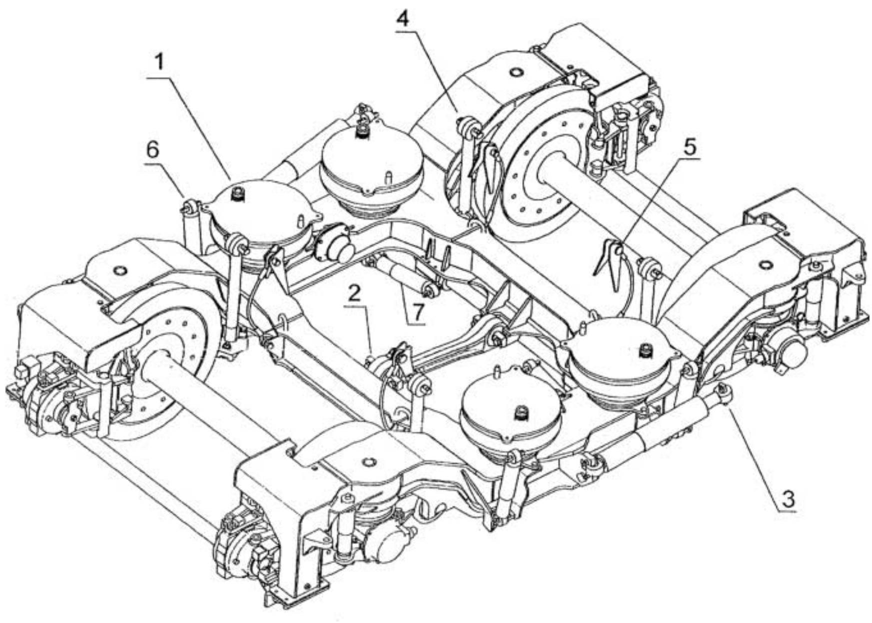

Figure 4. The Jacobs bogie.

The secondary suspension stage comprises the following elements:

- two airsprings (four in the Jacobs bogie) for the vertical, longitudinal and lateral stiffnesses, used to guarantee passengers' comfort and a simple automatic regulation of the coach height with changes in the vertical loads;
- a nonlinear longitudinal rod, to transmit the traction and braking efforts;
- a torsion bar, to provide the correct rolling stiffness;
- nonlinear lateral bump stops;
- nonlinear lateral dampers;
- nonlinear vertical dampers and
- nonlinear anti-yaw dampers.

Table 1. The main inertial properties of the Aln 501 Minuetto.

	Mass (kg)	I_{xx} (kg m^2)	I_{yy} (kg m^2)	I_{zz} (kg m^2)
External coach	31,568	66,700	764,000	743,000
Internal coach	14,496	30,600	245,000	236,000
Motor bogie frame	3306	1578	2772	4200
Trailer bogie frame	3122	1647	3453	5011
Wheelset	2091	1073	120	1073

Table 2. The main linear stiffness properties of the ALn 501 'Minuetto'.

Primary suspension	Flexicoil k_z	9.01E + 05 N/m
	Flexicoil k_x, k_y	1.26E + 06 N/m
	Bushing k_x	2.0E + 07 N/m
	Bushing k_y	1.5E + 07 N/m
Secondary suspension	Airspring k_z	3.98E + 05 N/m
	Airspring k_x, k_y	1.2E + 05 N/m
	Anti-roll bar k_α	2.6E + 06 Nm/rad
Coach connection	Bushing k_x, k_z	7.24E + 07 N/m
	Bushing k_y	5.2E + 06 N/m

The connection between two coaches consists of a stiffness element and a nonlinear damper that attenuates the relative lateral and roll motions. The resultant whole SIMPACK multibody model includes 31 rigid bodies: 3 coaches, 4 bogie frames, 8 wheelsets and 16 axle boxes. The most significant inertial properties of the model bodies are summarised in Table 1. All the kinematic constraints and the force elements have been modelled as viscoelastic force elements, taking into account all the mechanical nonlinearities (bump stop clearances, dampers and rod behaviour) [10,11]. In this regard, the main linear characteristics of the suspensions are summarised in Table 2; on the contrary, two examples of the nonlinear behaviour of the dampers of both stages of suspensions are shown in Figure 5.

3.2. *The global contact model*

The global contact model allows to perform an online calculation of the contact forces at the wheel–rail interface during the multibody simulations. At each time step, SIMPACK passes the kinematic data (wheelset position and orientation and their derivatives) to the global contact model, which evaluates the interaction forces to be applied to the wheels in the simulations. The new model is based on a semi-analytical approach that guarantees the following features ([12–14]):

- generic wheel and rail profiles can be implemented;
- fully 3D approach to the problem, with all degrees of freedom between the wheel and the rail taken into account;
- no simplifying hypotheses on the problem geometry and kinematics;
- multiple points of contact are allowed with no bounds to the their overall number and
- high numerical efficiency, which allows the online implementation directly within the multi-body models, without look-up tables; numerical performance better than those obtainable with commercial software (Vi-Rail™ and SIMPACK) [6–8].

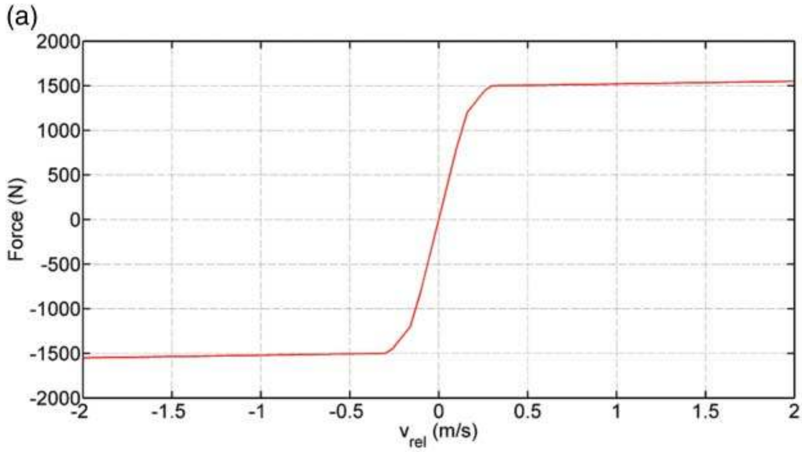

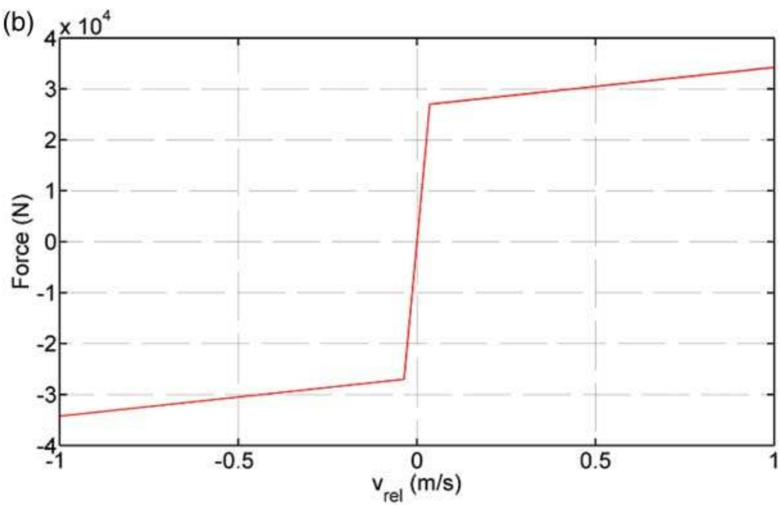

Figure 5. The nonlinear characteristic of the dampers: (a) vertical damper of the primary suspension and (b) anti-yaw damper of the secondary suspension.

The contact model action consists of two sequential phases: the research on the contact points and the computation of the normal and tangential actions in each contact patch.

3.2.1. *Research on the contact points*

The first task is entrusted to an algorithm developed by the authors in previous works (the DIST method [6,7]) that takes into account the original multi-dimensional contact problem (4D) and reduces it to a simpler scalar problem (1D), which can be easily handled by means of numerical methods, with remarkable advantages:

- the multiple solution management is simpler;
- a wide range of algorithms, even the elementary non-iterative ones, can efficiently resolve the numerical scalar problem (1D) and
- the convergence of iterative algorithms can be easily achieved and the algorithms converge to the solutions with fewer iterations and less computational effort.

In fact, with regard to the detection of the contact points, being the DIST algorithm based on a rigid approach, it is faster than the methods which take the zero-dimensional elasticity in the contact patches into consideration. It is obviously much faster than the algorithms based on the FEM approach in discretising the contact patches.

The detection algorithm is based on the standard idea that the distance between the wheel surface and the rail surface is stationary in the considered points [15,16]. The research requires to solve an algebraic system, whose formulation arises by imposing a few geometrical conditions. As can be seen in Figure 6, which shows the nomenclature for the coordinates of a point on the wheel, two reference systems are introduced to formulate the problem: the *auxiliary system* $O_r x_r y_r z_r$ and the *local system* $O_w x_w y_w z_w$. The first system moves along the track centreline following the wheelset: x_r is tangential to the centreline in the O_r point, while the z_r axis is perpendicular to the plane of track; the position of O_r can be determined imposing that the $y_r z_r$ plane contains the wheelset centre of mass G_w. The local system is fixed on the wheelset, except for the rotation around the wheelset axle: in particular, $O_w \equiv G_w$ and y_w coincides with the wheelset rotation axis. As can be seen in Figure 6, $\mathbf{p}_w^r$ and $\mathbf{p}_w^w$ are the positions of a point on the wheel in the auxiliary system and in the local system, respectively, while the position vector of a point on the rail surface in the auxiliary system is indicated with $\mathbf{p}_r^r$. At this point, the geometrical conditions can be stated as follows:

- the normal unitary vector relative to the rail surface $\mathbf{n}_r^r(\mathbf{p}_r^r)$ and the wheel surface unitary vector $\mathbf{n}_w^r(\mathbf{p}_w^r)$ have to be parallel ($\mathbf{R}_2$ is the rotation matrix that links the local system to the auxiliary one):

$$\mathbf{n}_r^r \times \mathbf{n}_w^r(\mathbf{p}_w^r) = \mathbf{n}_r^r(\mathbf{p}_r^r) \times \mathbf{R}_2 \mathbf{n}_w^w(\mathbf{p}_w^w) = \mathbf{0}; \tag{1}$$

  the wheel and rail surfaces can be locally considered as revolution and extrusion surfaces, respectively: $\mathbf{p}_w^{w\,T} = (x_w, y_w, -\sqrt{w(y_w)^2 - x_w^2})$, $\mathbf{p}_r^{r\,T} = (x_r, y_r, r(y_r))$, where the generative functions $w(y_w)$ and $r(y_r)$ are supposed to be known;

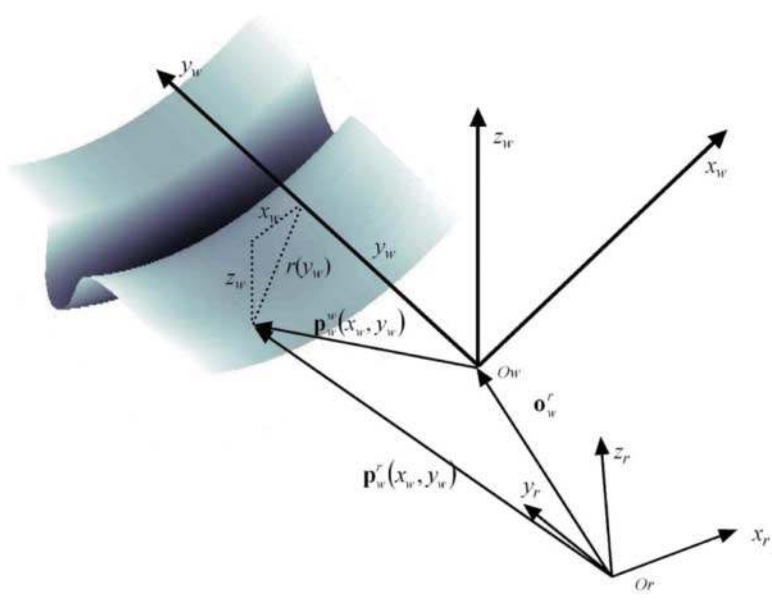

Figure 6. The coordinates of a point on the wheel surface.

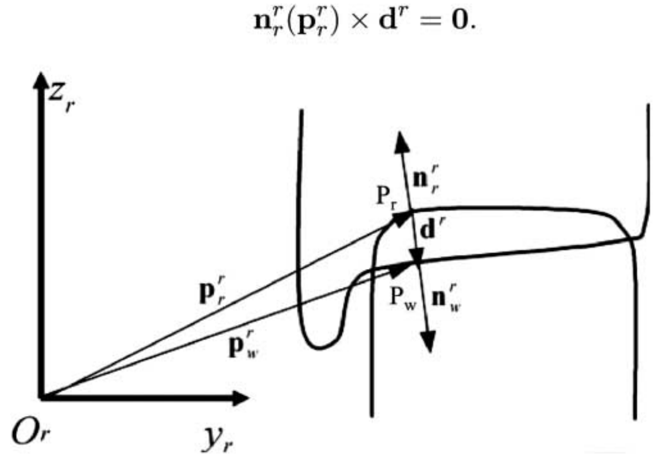

Figure 7. The distance method: vectors involved in the algorithm formulation.

- the rail surface normal unitary vector $\mathbf{n}_\mathrm{r}^\mathrm{r}(\mathbf{p}_\mathrm{r}^\mathrm{r})$ has to be parallel to the distance vector $\mathbf{d}^\mathrm{r} = \mathbf{p}_\mathrm{w}^\mathrm{r} - \mathbf{p}_\mathrm{r}^\mathrm{r}$ between the generic point of the wheel and of the rail (Figure 7):

$$\mathbf{n}_\mathrm{r}^\mathrm{r}(\mathbf{p}_\mathrm{r}^\mathrm{r}) \times \mathbf{d}^\mathrm{r} = \mathbf{0}. \tag{2}$$

Alternately, the problem can also be equivalently formulated imposing that the distance vector $\mathbf{d}^\mathrm{r}$ is perpendicular both to the wheel and to the rail tangent plane. Nevertheless, due to the particular structure of the algebraic equations, the calculation and the resolution algorithm are more complicated than the ones arising from Equations (1) and (2).

The distance between the generic points on the wheel and on the rail can be expressed as

$$\mathbf{d}^\mathrm{r}(x_\mathrm{w}, y_\mathrm{w}, x_\mathrm{r}, y_\mathrm{r}) = \mathbf{p}_\mathrm{w}^\mathrm{r}(x_\mathrm{w}, y_\mathrm{w}) - \mathbf{p}_\mathrm{r}^\mathrm{r}(x_\mathrm{r}, y_\mathrm{r}) = \mathbf{o}_\mathrm{w}^\mathrm{r} + \mathbf{R}_2\mathbf{p}_\mathrm{w}^{w}(x_\mathrm{w}, y_\mathrm{w}) - \mathbf{p}_\mathrm{r}^\mathrm{r}(x_\mathrm{r}, y_\mathrm{r}) \tag{3}$$

thus, it depends on the four parameters $(x_\mathrm{w}, y_\mathrm{w}, x_\mathrm{r}, y_\mathrm{r})$ that identify a point on both the surfaces. Equations (1) and (2) constitute a system with six scalar equations and four unknowns $(x_\mathrm{w}, y_\mathrm{w}, x_\mathrm{r}, y_\mathrm{r})$ (only four of the equations are independent). As stated previously, the problem can be reduced to a scalar equation in the unknown y_w expressing x_w, x_r and y_r as functions of y_w. The second component of Equation (1) gives

$$r_{13}\sqrt{r(y_\mathrm{w})^2 - x_\mathrm{w}^2} = r_{11}x_\mathrm{w} - r_{12}r(y_\mathrm{w})r'(y_\mathrm{w}), \tag{4}$$

where r_{13}, r_{11} and r_{12} are elements of the $\mathbf{R}_2$ matrix. If $A = r_{13}$, $B = r(y_\mathrm{w})$, $C = r_{11}$ and $D = r_{12}r(y_\mathrm{w})r'(y_\mathrm{w})$, the previous equation becomes

$$A\sqrt{B^2 - x_\mathrm{w}^2} = Cx_\mathrm{w} - D. \tag{5}$$

Removing the radical and solving for x_w, the following expression can be written as

$$x_{\mathrm{w}1,2}(y_\mathrm{w}) = \frac{CD \pm \sqrt{C^2D^2 - (C^2 + A^2)(D^2 - A^2B^2)}}{C^2 + A^2}; \tag{6}$$

therefore, there are two possible values x_w for each y_w. Moreover, substituting $x_{\mathrm{w}1,2}(y_\mathrm{w})$ in the first component of Equation (1), an expression for the rail profile derivative can be obtained

$$b'(y_\mathrm{r})_{1,2} = \frac{r_{21}x_{\mathrm{w}1,2}(y_\mathrm{w}) - r_{22}r(y_\mathrm{w})r'(y_\mathrm{w}) - r_{23}\sqrt{r(y_\mathrm{w})^2 - x_{\mathrm{w}1,2}(y_\mathrm{w})^2}}{r_{32}r(y_\mathrm{w})r'(y_\mathrm{w}) + r_{33}\sqrt{r(y_\mathrm{w})^2 - x_{\mathrm{w}1,2}(y_\mathrm{w})^2}}. \tag{7}$$

Considering both the track sides separately, if $b'(y_r)_{1,2}$ is decreasing monotonously, Equation (7) is numerically invertible, giving $y_{r1,2}$. Otherwise, the numerical inversion will be possible anyway, but it will produce a further multiplication of the solution number. Finally, the second scalar component of Equation (2) can be rewritten as

$$x_{r1,2}(y_w) = r_{11}x_{w1,2}(y_w) + r_{12}y_w - r_{13}\sqrt{r(y_w)^2 - x_{r1,2}(y_w)^2}. \tag{8}$$

At this point, the values of the three variables x_w, x_r and y_r can now be substituted in the first component of Equation (2), to write the following relation

$$\begin{aligned} F_{1,2}(y_w) = {} & -b'(y_{r1,2}(y_w))(G_z + r_{32}y_w - r_{33}\sqrt{r(y_w)^2 - x_{w1,2}(y_w)^2} - b(y_{r1,2}(y_w))) \\ & - (G_y + r_{21}x_{w1,2}(y_w) + r_{22}y_w - r_{23}\sqrt{r(y_w)^2 - x_{w1,2}(y_w)^2} - y_{r1,2}(y_w)) = 0; \end{aligned} \tag{9}$$

Equations (9) are two simple scalar equations in the y_w variable, easy to resolve numerically with the advantages mentioned previously (in the following, y^C_{w1j} and y^C_{w2k} with $1 \le j \le n_1$ and $1 \le k \le n_2$ will be the generic solution of $F_1(y_w) = 0$ and $F_2(y_w) = 0$, respectively). In this way, the dimension of the initial problem has been reduced from four to one, as discussed earlier. For each y^C_w, the values of the unknowns x^C_w, x^C_r and y^C_r and, consequently, the contact point positions on the wheel and the rail $\mathbf{p}^{r,C}_w = p^r_w(x^C_w, y^C_w)$ and $\mathbf{p}^{r,C}_r = p^r_r(x^C_r, y^C_r)$ can be determined by substitution.

Since the equation includes irrational terms, a root can be accepted only if it satisfies all the following analytical conditions:

- x^C_{w1j} and x^C_{w2k} (calculated by Equation (6) for y^C_{w1j} and y^C_{w2k}) have to be real numbers;
- the terms $\sqrt{r(y^C_{w1j})^2 - x(y^C_{w1j})^2}$ and $\sqrt{r(y^C_{w2k})^2 - x(y^C_{w2k})^2}$ of Equation (9) have to be real too and
- (x^C_{w1j}, y^C_{w1j}) and (x^C_{w2k}, y^C_{w2k}) have to be effective solutions of Equation (4), considering the radical removing;

The following physical conditions also have to be respected so that the contact is physically possible:

- the penetration between the wheel and rail surfaces ($p_n = \mathbf{d}^r \cdot \mathbf{n}^r_r$) has to be less or equal to zero, according to the adopted nomenclature;
- multiple solutions have to be rejected and
- the normal curvatures of the wheel and the rail surfaces in the longitudinal and lateral directions ($k^C_{1,wi}$, $k^C_{1,wi}$, $k^C_{2,ri}$, $k^C_{2,ri}$), evaluated in the contact points, have to satisfy the convexity condition in order to make the contact physically possible ($k^C_{1,wi} + k^C_{1,ri} > 0$; $k^C_{2,wi} + k^C_{2,ri} > 0$).

3.2.2. *Evaluation of the contact forces*

The calculation of the contact forces for each contact point is based on a semi-elastic approach which uses both Hertz's and Kalker's global theories. The normal contact force, according to Hertz's theory, depends both on the penetration p_n between the surface of wheel and the rail and on the penetration velocity $v_n = \mathbf{v} \cdot \mathbf{n}^r_r(\mathbf{p}^{r,C}_r)$, where $\mathbf{v}$ is the contact point velocity,

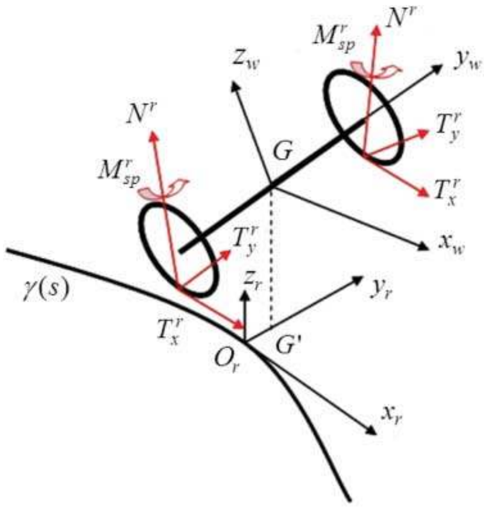

Figure 8. The nomenclature of the contact forces.

assuming that it is rigidly connected to the wheel:

$$N^{\mathrm{r}}(\mathbf{p}_{\mathrm{r}}^{\mathrm{r,C}}) = \left[-k_h|p_n|^{\gamma} + k_v|v_n|\frac{\mathrm{sgn}(v_n)-1}{2}\right]\frac{\mathrm{sgn}(p_n)-1}{2}, \tag{10}$$

where γ is equal to $3/2$, k_h is Kalker's stiffness constant depending on the surface geometries and the material properties and k_v is a damping contact constant [9]. The same theory also allows to evaluate the contact patch semiaxes a, b and the ellipse eccentricity.

Linear Kalker's theory is then applied to calculate the tangential forces and the spin moment (Figure 8) in each contact patch:

$$\begin{aligned} T_x^{\mathrm{r}}(\mathbf{p}_{\mathrm{r}}^{\mathrm{r,C}}) &= -f_{11}\xi_x, \\ T_y^{\mathrm{r}}(\mathbf{p}_{\mathrm{r}}^{\mathrm{r,C}}) &= -f_{22}\xi_y - f_{23}\xi_{\mathrm{sp}}, \\ M_{\mathrm{sp}}^{\mathrm{r}}(\mathbf{p}_{\mathrm{r}}^{\mathrm{r,C}}) &= -f_{23}\xi_y - f_{33}\xi_{\mathrm{sp}}, \end{aligned} \tag{11}$$

where the value of the f_{ij} coefficients, which are the functions of the material properties and the ellipse semiaxis, can be found in the literature [9]. ξ_x, ξ_y and ξ_{sp} are the longitudinal, lateral and the spin creepages, as defined below:

$$\xi_x = \frac{\mathbf{v}\cdot\mathbf{i}_{\mathrm{r}}}{\|\dot{G}_{\mathrm{w},f}^{\mathrm{r}}\|}; \quad \xi_y = \frac{\mathbf{v}\cdot\mathbf{t}_{\mathrm{r}}^{\mathrm{r}}}{\|\dot{G}_{\mathrm{w},f}^{\mathrm{r}}\|}; \quad \xi_{\mathrm{sp}} = \frac{\boldsymbol{\omega}^{\mathrm{r}}\cdot\mathbf{n}_{\mathrm{r}}^{\mathrm{r}}}{\|\dot{G}_{\mathrm{w},f}^{\mathrm{r}}\|}, \tag{12}$$

where $\dot{G}_{\mathrm{w},f}^{\mathrm{r}}$ is the absolute velocity of the wheelset centre of mass, $\mathbf{i}_{\mathrm{r}}$ is the unit vector of the x_{r} axis, $\boldsymbol{\omega}^{\mathrm{r}}$ is the wheelset angular velocity expressed in the auxiliary reference system and $\mathbf{t}_{\mathrm{r}}^{\mathrm{r}} = \mathbf{n}_{\mathrm{r}}^{\mathrm{r}} \times \mathbf{i}_{\mathrm{r}}$.

Since Kalker's theory is linear, to include the effect of the adhesion limit due to friction, a saturation criterion has to be introduced in the model to limit the magnitude of the tangential contact force $\tilde{T}^{\mathrm{r}} = \sqrt{\tilde{T}_x^{\mathrm{r}^2} + \tilde{T}_y^{\mathrm{r}^2}}$, which cannot exceed the slip value $T_{\mathrm{s}}^{\mathrm{r}} = \mu N^{\mathrm{r}}$. Therefore, a saturation coefficient ϵ (Equation 13) is defined according to the Shen–Hedrick–Elkins formulation [10]:

$$\epsilon = \begin{cases} \dfrac{\mu N^{\mathrm{r}}}{\tilde{T}^{\mathrm{r}}}\left[\left(\dfrac{\tilde{T}^{\mathrm{r}}}{\mu N^{\mathrm{r}}}\right) - \dfrac{1}{3}\left(\dfrac{\tilde{T}^{\mathrm{r}}}{\mu N^{\mathrm{r}}}\right)^2 + \dfrac{1}{27}\left(\dfrac{\tilde{T}^{\mathrm{r}}}{\mu N^{\mathrm{r}}}\right)^3\right] & \text{if } \tilde{T}^{\mathrm{r}} \leq 3\mu N^{\mathrm{r}}, \\ \dfrac{\mu N^{\mathrm{r}}}{\tilde{T}^{\mathrm{r}}} & \text{if } \tilde{T}^{\mathrm{r}} > 3\mu N^{\mathrm{r}}, \end{cases} \tag{13}$$

in this way, the saturated tangential force will be $\mathbf{T}^{\mathrm{r}} = \epsilon\tilde{T}^{\mathrm{r}}$.

4. The wear evaluation

4.1. *The local contact model*

The local contact model starts from the global contact variables evaluated by the vehicle model (contact point positions, contact forces and spin moments, global creepages and patch semiaxes) and calculates the local contact variables (normal pressures, tangential stresses and creepages) within each contact patch. The model is based on an approximate but very efficient version of Kalker's local theory implemented in his FASTSIM algorithm [9], commonly used in railway multibody simulations. The algorithm works in a local reference system, whose origin is situated at the centre of the elliptical contact path, with the x and y axes defined in the common tangent plane to the contact surfaces, as shown in Figure 9; therefore, they are not parallel to either the local reference system of the wheelset or the auxiliary system.

The working hypothesis on which the algorithm is developed is the proportionality between the tangential pressure $\mathbf{p}_{\mathrm{t}}$ and the elastic displacement $\mathbf{u}$ in a generic point of the contact patch:

$$\mathbf{u}(x,y) = L\mathbf{p}_{\mathrm{t}}(x,y), \quad L = L(\boldsymbol{\xi}, a, b, G, \nu), \tag{14}$$

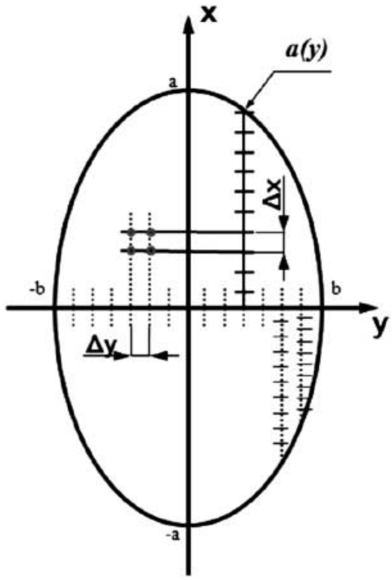

Figure 9. The contact patch discretisation in the FASTSIM algorithm.

where the flexibility L is a function of the global creepage vector $\boldsymbol{\xi}$, the ellipse semiaxes a, b, the combined shear modulus G and the combined Poisson's coefficient ν, as expressed below:

$$L = \frac{|\xi_x|L_1 + |\xi_y|L_2 + c|\xi_{\mathrm{sp}}|L_3}{\sqrt{\xi_x^2 + \xi_y^2 + c^2\xi_{\mathrm{sp}}^2}}, \tag{15}$$

in which $L_1 = 8a/(3Gc_{11})$, $L_2 = 8a/(3Gc_{22})$, $L_3 = \pi a^2/(4Gcc_{23})$ and $c = \sqrt{ab}$. Kalker's parameters c_{ij}, which are functions of a/b and ν, can be easily found tabulated in the literature.

The local creepages in a generic point can be obtained by deriving the elastic displacements and considering both the rigid global creepages and the vehicle speed V:

$$\boldsymbol{\sigma}(x, y) = \dot{\mathbf{u}}(x, y) + V \begin{bmatrix} \xi_x \\ \xi_y \end{bmatrix}. \tag{16}$$

The calculation of the local variables p_n, $\mathbf{p}_t$ and $\boldsymbol{\sigma}$ is performed in each point of the grid adopted to mesh the contact patch (Figure 9): the transversal axis of the contact ellipse, with respect to the travelling direction, is divided into $n_y - 1$ parts with a length of $\Delta y = 2b/(n_y - 1)$ by means of n_y equidistant nodes. Similarly, the longitudinal sections of the patch which are $2a(y) = 2a\sqrt{1 - (y/b)^2}$ long are divided into $n_x - 1$ equal parts of $\Delta x(y) = 2a(y)/(n_x - 1)$ length using n_x equidistant nodes. This choice leads to a non-constant longitudinal resolution which increases nearby the lateral edges of the ellipse, where the length $a(y)$ is shorter. So, the accuracy near the edge is appreciably higher than that obtainable with a constant resolution grid that would produce more numerical errors. The n_x and n_y parameters have to be chosen as a compromise between numerical efficiency and precision; the range $25 \div 50$ has proven to work fine. The expressions of the normal pressure and the adhesion limit pressure in a generic point (x_h, y_l) of the grid, with $1 \le h \le n_x$, $1 \le l \le n_y$, are as follows:

$$p_n(x_h, y_l) = \frac{3}{2}\frac{N^{\mathrm{r}}}{\pi ab}\sqrt{1 - \frac{x_h^2}{a^2} - \frac{y_l^2}{b^2}}; \tag{17}$$

$$\mathbf{p_A}(x_h, y_l) = \mathbf{p_t}(x_h - \Delta x(y_l), y_l) - \begin{bmatrix} \xi_x \\ \xi_y \end{bmatrix}\frac{\Delta x(y_l)}{L} = \mathbf{p_t}(x_{h-1}, y_l) - \begin{bmatrix} \xi_x \\ \xi_y \end{bmatrix}\frac{\Delta x(y_l)}{L}, \tag{18}$$

where N^{r} is the normal contact force. Starting from the values of the local variables in (x_{h-1}, y_l), the algorithm works iteratively to find the exact distribution of the local variables in (x_h, y_l):

$$\|\mathbf{p_A}(x_h, y_l)\| \le \mu p_n(x_h, y_l) \Rightarrow \mathbf{p_t}(x_h, y_l) = \mathbf{p_A}(x_h, y_l), \quad \boldsymbol{\sigma}(x_h, y_l) = \mathbf{0}, \tag{19}$$

$$\|\mathbf{p_A}(x_h, y_l)\| > \mu p_n(x_h, y_l) \Rightarrow \begin{cases} \mathbf{p_t}(x_h, y_l) = \mu p_n(x_h, y_l)\mathbf{p_A}(x_h, y_l)/\|\mathbf{p_A}(x_h, y_l)\|, \\ \boldsymbol{\sigma}(x_h, y_l) = \dfrac{LV}{\Delta x(y_l)}(\mathbf{p_t}(x_h, y_l) - \mathbf{p_A}(x_h, y_l)), \end{cases} \tag{20}$$

where the boundary conditions are $\mathbf{p_t}(x_1, y_l) = \mathbf{0}$, $\boldsymbol{\sigma}(x_1, y_l) = \mathbf{0}$, $1 \le l \le n_y$, since creepages and pressures have to be zero outside the contact patch. Finally, the distributions of the pressures $p_n(x_h, y_l)$ and $\mathbf{p_t}(x_h, y_l)$ and the creepages $\boldsymbol{\sigma}(x_h, y_l)$ are found by iterating the procedure for $2 \le h \le n_x$ and $1 \le l \le n_y$.

4.2. *The wear model*

As discussed in the previous sections, the following working hypotheses have been introduced to approach the problem:

- the wear affects only the wheels, while the rails keep their original unworn profile during the whole process;
- the wear is evaluated according to a law that is experimentally proven [3,5];
- the output of the wear model is a single mean wheel profile to be used in the next step, which includes the effect of the wear on all the wheels of the vehicle, and
- dry conditions in the wheel–rail interface.

With regard to the first point, the logical approach to the problem and its modelling can easily be extended, involving the case of the worn constant rail profile and even the simulation of the rail profile evolution.

As stated previously, the calculation of the wear on the wheel is based on an experimental law according to which the volume of the removed material correlates with the total frictional work. The main output of the wear model is the specific volume $\delta_{P_i^{jk}(t)}(x, y)$, expressed in $\mathrm{mm}^3/(\mathrm{mm}^2\mathrm{m})$, a function of time which describes the specific volume (the volume per unit of area and per unit of travelled distance) of the material to be removed in the grid position (x, y) of the contact patch $P_i^{jk}(t)$. The integral with respect to x and y over the grid gives the specific volume of the removed material per unit of travelled distance relative to the contact patch $P_i^{jk}(t)$. In fact, the subscript $P_i^{jk}(t)$ indicates the contact patch ith of the wheel jth in the kth multibody simulation of the statistical analysis of the track. With regard to the statistical approach, the track and its features will be explained in the next section. The three indexes just introduced are variable in the following intervals:

- $1 \leq j \leq N_\mathrm{W}$, where N_W is the number of wheels of the vehicle,
- $1 \leq i \leq N_\mathrm{P}$, where N_P is the maximum allowed number of contact points (as will be explained below), and
- $1 \leq k \leq N_\mathrm{C}$, with N_C being equal to the number of multibody simulations in the statistical description of the real track.

The quantity $\delta_{P_i^{jk}(t)}(x, y)$ has to be evaluated in each point (x_h, y_l) of the contact patch grid. To this end, the local frictional power in these points can be estimated by means of the *wear index* $I_\mathrm{W}(\mathrm{N/mm}^2)$:

$$I_\mathrm{W} = \frac{\mathbf{p_t} \cdot \boldsymbol{\sigma}}{V}, \tag{21}$$

which is experimentally related (Figure 10) to the *wear rate* K ($\mu\mathrm{g/m{\cdot}mm}^2$): the wear rate gives a measure of the amount of material removed per metre of travelled distance (m) travelled by the train and per mm^2 of surface. The analytical expression for $K(I_\mathrm{W})$ is given by Equation (22). These data, arising from experimental tests conducted on a roller rig and concerning the case of a steel–steel contact under dry conditions, are available in the literature [3,5]:

$$K_\mathrm{W}(I_\mathrm{W}) = \begin{cases} 5.3 \cdot I_\mathrm{W}, & I_\mathrm{W} < 10.4\ \mathrm{N/mm}^2, \\ 55.0, & 10.4 \leq I_\mathrm{W} \leq 77.2\ \mathrm{N/mm}^2\ , \\ 61.9 \cdot I_\mathrm{W} - 4723, & I_\mathrm{W} > 77.2\ \mathrm{N/mm}^2. \end{cases} \tag{22}$$

Normally, the wear rate on the tread is typically $K1$, while on the flange both the $K1$ and $K2$ regimes occur. In this regard, Figures 11 and 12 show an example of the frequency distribution of the two wear regimes along the lateral coordinate of the mean wheel profile (after taking the average on wheels and simulations), arising from a few operations described in Section 4.3.

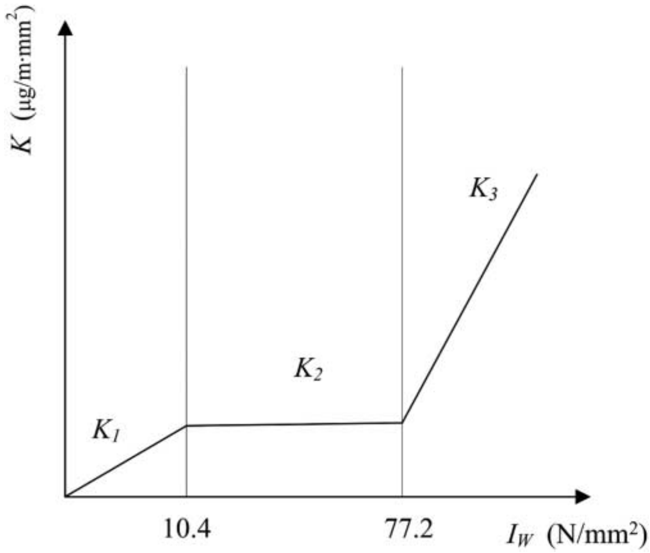

Figure 10. The wear rate as a function of wear index.

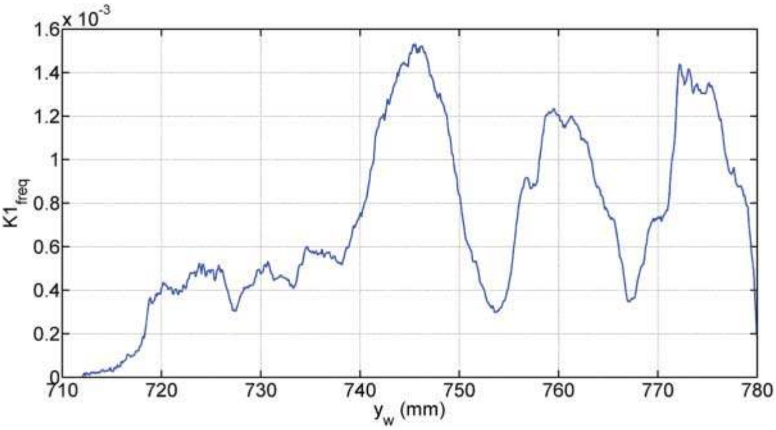

Figure 11. Typical frequency distribution of the $K1$ wear regime after taking the average on wheels and simulations (Section 4.3).

After evaluating the wear rate, the specific volume $\delta_{P_i^{jk}(t)}(x, y)$ can be calculated as follows:

$$\delta_{P_i^{jk}(t)}(x, y) = \frac{K(I_W)}{\rho} \quad \left(\frac{\mathrm{mm}^3}{\mathrm{m\ mm}^2}\right), \tag{23}$$

where ρ is the material density (expressed in $\mathrm{kg/m^3}$). The numerical wear rate arising from the model could be different from the real overall rate if the effects of plastic or fatigue wear were remarkable. A further tuning of the model, acting on the filter used in each step of the procedure to smooth the wheel profiles, could compensate possible differences in the comparison with experimental data. Therefore, as will be clarified below, the filter has two purposes: it cuts the noise in the distribution of removed material, erasing the physically meaningless short spatial wavelengths in the profile that would cause problems to the global contact model and moreover

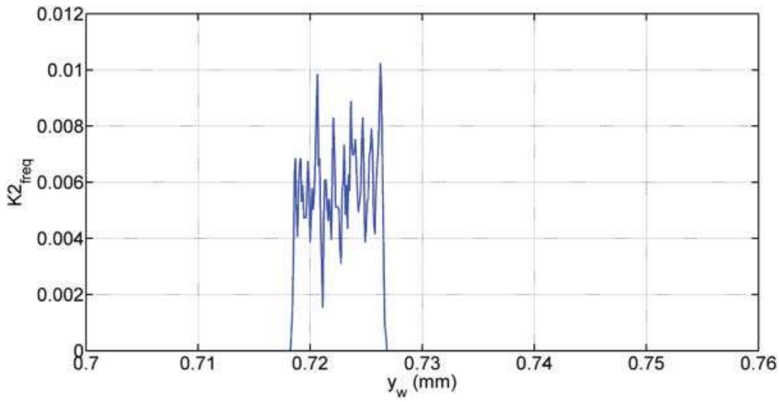

Figure 12. Typical frequency distribution of the $K2$ wear regime after taking the average on wheels and simulations (Section 4.3).

it could allow the reduction of the errors related to the presence of other wear mechanisms (i.e. the plastic and fatigue wear).

4.3. *The profile update*

The profile update is the part of the whole architecture which provides, by means of numerical procedures, the wheel profile for the next step $r_n(y_{\mathrm{w}})$ starting from the profile used at the current step $r_{\mathrm{p}}(y_{\mathrm{w}})$ and exploiting the results of the wear model. It is surely a key point of the procedure since the adopted strategy may appreciably affect the results. The importance of this task lies in the following issues:

- The wear model, according to the working hypotheses, has to generate a single wheel profile as an output, taking into account the data relative to all the wheels of the vehicle. A single function of the material to be removed has to be obtained from the analysis of all the contact patches.
- Due to the discrete approach to the wheel geometry update, the distribution $\delta_{P_i^{jk}(t)}(x,y)$ presents quite a considerable numerical noise and needs to be treated to avoid, as stated previously, a non-physical profile with short spatial wavelengths, which may not be handled by the global contact model.

With regard to the first point, the whole model can easily handle different wheel profiles to distinguish the wear evolution of each wheel. Nevertheless, the average of the profile on all the wheels has been adopted to meet the requirements of the research project issued by Trenitalia S.p.A (one single wheel profile as an output of the whole wear model), which aims at a wheel profile optimisation in future. The numerical procedures which provide the new profile are described below:

(1) Longitudinal integration:

$$\frac{1}{2\pi w(y_i^{jk})}\int_{-a(y)}^{a(y)} \delta_{P_i^{jk}(t)}(x,y)\mathrm{d}x = \delta^{\mathrm{tot}}_{P_i^{jk}(t)}(y) \quad \left(\frac{\mathrm{mm}^3}{\mathrm{m\ mm}^2}\right), \tag{24}$$

this operation sums all the wear contributions in the longitudinal direction and spreads them along the circumference of radius $w(y_i^{jk})$.

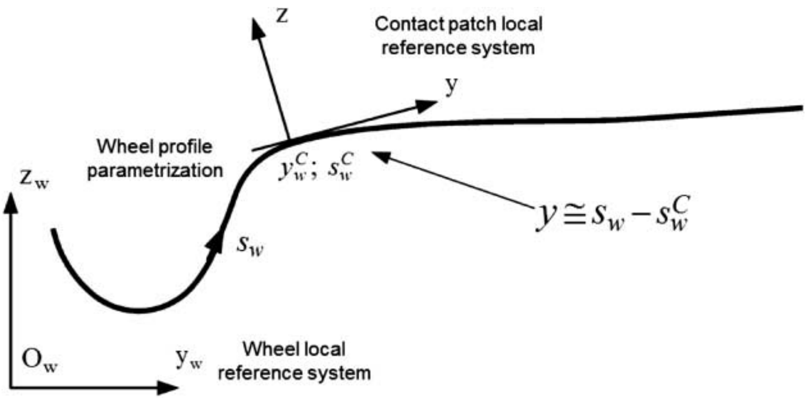

Figure 13. Wheel profile parametrisation.

(2) Time integration:

$$\int_{T_i}^{T_f} \delta^{\text{tot}}_{P_i^{jk}(t)}(s_\text{w} - s_{\text{w}i}^{jk,\text{C}}(t))V(t)\,\text{d}t \cong \Delta_{P_i^{jk}}(s_\text{w}) \quad (\text{mm}), \tag{25}$$

where $y \cong s_\text{w} - s_{\text{w}i}^{jk,\text{C}}$ (Figure 13), s_w is the generic curvilinear abscissa, $s_{\text{w}i}^{jk,\text{C}}(t)$ is the curvilinear abscissa of the contact point on the wheel at the time t and $V(t)$ is the vehicle speed. The integration performs the sum of all the contributions during the dynamic simulation: the result is the depth of the material to be removed due to the considered contact point.

(3) Sum of the contact points:

$$\sum_{i=1}^{N_\text{P}} \Delta_{P_i^{jk}}(s_\text{w}) = \Delta_{jk}(s_\text{w}), \tag{26}$$

where N_P is the above-mentioned maximum number of contact points on a single wheel (a parameter of the global contact model) and $\Delta_{jk}(y_\text{w})$ is the removed material of the jth wheel during the kth dynamic simulation. The contact patches are usually less than N_P and their number can vary during the simulation; hence, since the summation is extended to N_P, the contribution of the missing points has been automatically set to be equal to zero.

(4) Average on the wheels and the simulations:

$$\sum_{i=1}^{N_\text{C}} p_k \frac{1}{N_\text{W}} \sum_{j=1}^{N_\text{W}} \Delta_{jk}(s_\text{w}) = \bar{\Delta}(s_\text{w}); \tag{27}$$

this operation involves the average on the N_W wheels and the weighted average on the N_C simulations. As explained in the next section, p_k, $1 \leq k \leq N_\text{C}$, $\sum_{i=1}^{N_\text{C}} p_k = 1$ are the normalised weights related to the simulations of the statistical analysis to differentiate the relative impact on the wear of each track; the relative weights are chosen on the basis of the frequency with which the curved track appears in the Aosta–Pre Saint Didier railway line.

(5) Scaling of the mileage:
Since an appreciable evolution of the wheel profile requires thousands of kilometres to manifest itself, the scaling of the distance becomes critically important to get results in a reasonable time. Although the real chosen mileage km_tot that the vehicle has to run is

Figure 14. Partitioning of the total distance to be run in discrete steps.

divided into discrete steps of length $\mathrm{km_{step}}$ (Figure 14), the step length is excessive anyway for the multibody approach and thus the scaling of Equation (28) is adopted:

$$\bar{\Delta}(s_w)\frac{\mathrm{km_{step}}}{\mathrm{km_{runs}}} = \bar{\Delta}^{sc}(s_w). \tag{28}$$

In fact, the amount of removed material $\bar{\Delta}(s_w)$ depends on the overall mileage travelled by the vehicle during the N_C simulations, that is, $\mathrm{km_{runs}} = L_C$, where L_C is the length of curved tracks on which the results of the vehicle dynamics are extrapolated. As described previously, if the numerically simulated track is a significant statistical representation of the track associated with the discrete spatial step, the adopted working hypothesis is reasonable. The proportionality is exploited only within a distance equal to $\mathrm{km_{step}}$ and the nonlinearity of the physical problem is preserved.

After the scaling, the quantity $\bar{\Delta}^{sc}(s_w)$ is related to a spatial step with a length equal to $\mathrm{km_{step}}$, instead of $\mathrm{km_{runs}}$. However, even though the scaling reduces the total computational time conveniently, the choice of $\mathrm{km_{step}}$ (and hence the number of steps, once $\mathrm{km_{tot}}$ is fixed) strongly affects the results and has to be made properly as a compromise between numerical efficiency and accuracy. In fact, a high number of steps leads to an accurate description of the phenomenon, requiring relevant computational efforts, while a large $\mathrm{km_{step}}$ increases the effect due to the discrete approach and amplifies the relative importance of the filter action and the numerical profile treatment on the final results.

For this reason, if $\mathrm{km_{step}}$ is constant, it must be chosen sufficiently shorter than $\mathrm{km_{tot}}$; otherwise, it can be set variable according to adaptive procedures (based, for example, on thresholds on the maximum of the removed material function $\bar{\Delta}^{sc}(s_w)$). During the validation of the model with the experimental data of the Aosta–Pre Saint Didier railway line, both the strategies were tested before choosing the constant step. In fact, in this scenario, with a low overall mileage, it provides comparable results in terms of accuracy and better performance from a numerical point of view.

(6) Smoothing of the amount of removed material:

$$\Im[\bar{\Delta}^{sc}(s_w)] = \bar{\Delta}^{sc}_{sm}(s_w). \tag{29}$$

This procedure aims at the following targets:
- model tuning,
- compensation to include other wear mechanisms,
- numerical noise filtering and
- removal of physically meaningless short spatial wavelengths.

In fact, depending on the choice of parameters, the filter could contribute to the agreement with experimental data, but it has not been used by the authors in this sense as a tuning tool. On the contrary, it has been exploited only to cut the numerical noise as highlighted by the difference between numerical results and experimental data (slightly underestimated) due to the presence of other wear mechanisms. To this end, the numerical noise and the short wavelength contributions are treated with a first-order discrete filter [17]: a moving mean with a window width equal to 1–5% of the total points that discretise the wheel profile.

This solution is simple and at the same time the filter does not change the total mass of the removed material, as obviously required.

(7) Profile update:

$$\begin{pmatrix} y_{\mathrm{w}}(s_{\mathrm{w}}) \\ r_{\mathrm{p}}(y_{\mathrm{w}}(s_{\mathrm{w}})) \end{pmatrix} - \bar{\Delta}^{s}_{\mathrm{sm}}(s_{\mathrm{w}})\mathbf{n}^{\mathrm{r}}_{\mathrm{r}} \xrightarrow{\text{re-parametrisation}} \begin{pmatrix} y_{\mathrm{w}}(s^{*}_{\mathrm{w}}) \\ r_{n}(y_{\mathrm{w}}(s^{*}_{\mathrm{w}})) \end{pmatrix}. \tag{30}$$

Finally, the profile for the next step is obtained by removing the material in the normal direction from the current profile $r_{\mathrm{p}}(s_{\mathrm{w}})$ (according to the function $\bar{\Delta}^{s}_{\mathrm{sm}}(s_{\mathrm{w}})$) and then by performing a new parametrisation, to get again a curve parametrised by means of the curvilinear abscissa.

5. Statistical approach to the track – model validation

This section is mainly dedicated to the explanation of the statistical analysis of the track and the discussion of the results of the work, in terms of model validation, including the treatment of the available experimental data.

5.1. *The Aosta–Pre Saint Didier railway line*

The statistical approach to the track has been chosen to reduce and rationalise the total simulation work, avoiding excessively long simulations on the real track. The idea is to substitute the simulation on the whole track with an equivalent set of simulations on short curved tracks, each of them with its own radius and superelevation. More precisely, the steps performed to get the statistical representation are as follows:

- a set of radius curve intervals characterised by a minimum R_{min} and a maximum R_{max} were identified analysing the database provided by RFI;
- each of these intervals was furthermore divided into superelevation subclasses, each of them with its own h_{min} and h_{max};
- for each subclass, a representative radius R_{m} was calculated as a weighted average on all the curve radii included in that subclass using the length of the curve as a weighting factor;
- the correspondent representative superelevation h was chosen as the most frequent superelevation among the values found in that class;
- for each subclass, a speed value V was chosen as the minimum value between the maximum speed allowable (depending on the radius, the superelevation and vehicle characteristics) and the speed calculated imposing a non-compensated acceleration of $0.6\,\mathrm{m/s^2}$;
- a weighting factor p_k was introduced for each subclass to take into account the frequency of certain matching radius and superelevation in the track and to diversify the wear contributions of the different curves and
- the transition lengths of the real track were not considered; hence, the wear was numerically evaluated on curves and straight tracks only.

A similar procedure turns out to be particularly useful if the wear analysis has to be performed on a complex railway net made up of long tracks.

The statistical approach to the Aosta–Pre Saint Didier railway line provided the classification given in Table 3, made up of N_{C} different classes (17 curves and the straight track). The results are summarised in the last four columns: the mean curve radius R_{m}, the representative superelevation h, the travelling speed V and the percentage weight p_k,

Table 3. The N_C tracks of the statistical approach.

R_{min} (m)	R_{max} (m)	Superelevation class $h_{min} - h_{max}$ (mm)	R_m (m)	h (mm)	V (km/h)	p_k (%)
147.1	156.3	0	–	–	–	–
		10–40	–	–	–	–
		60–80	–	–	–	–
		90–120	150	120	55	0.77
		130–160	–	–	–	–
156.3	166.7	0	–	–	–	–
		10–40	–	–	–	–
		60–80	–	–	–	–
		90–120	160	110	55	0.48
		130–160	165	140	55	0.56
166.7	178.6	0	–	–	–	–
		10–40	–	–	–	–
		60–80	–	–	–	–
		90–120	170	110	55	0.82
		130–160	175	130	55	1.55
178.6	192.3	0	–	–	–	–
		10–40	–	–	–	–
		60–80	–	–	–	–
		90–120	190	100	55	8.37
		130–160	180	130	55	0.45
192.3	208.3	0	–	–	–	–
		10–40	–	–	–	–
		60–80	–	–	–	–
		90–120	200	90	55	20.64
		130–160	200	130	60	4.00
208.3	227.3	0	–	–	–	–
		10–40	–	–	–	–
		60–80	220	80	55	0.70
		90–120	220	100	55	3.76
		130–160	–	–	–	–
227.3	250.0	0	–	–	–	–
		10–40	–	–	–	–
		60–80	240	80	55	7.26
		90–120	240	110	60	5.28
		130–160	–	–	–	–
250.0	312.5	0	–	–	–	–
		10–40	–	–	–	–
		60–80	270	70	55	3.91
		90–120	270	90	60	5.29
		130–160	–	–	–	–
312.5	416.7	0	–	–	–	–
		10–40	–	–	–	–
		60–80	370	60	55	2.26
		90–120	345	100	70	1.63
		130–160	–	–	–	–
416.7	∞	0	∞	0	70	32.27

$1 \leq k \leq N_C$. Blank rows are present because no curves were found for certain classes. The classification also highlights the sharpness of the track: the curve radii are less than or equal to about 400 m for two-thirds of it and thus the maximum speed is equal to $V_{max} = 70\,\text{km/h}$.

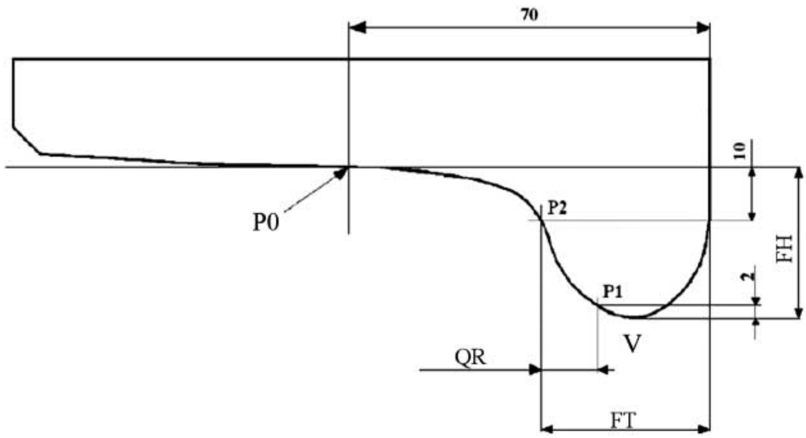

Figure 15. The reference dimensions of the wheel profile.

km	flange dimensions	1 r	1 l	2 r	2 l	3 r	3 l	4 r	4 l	5 r	5 l	6 r	6 l	7 r	7 l	8 r	8 l
		wheel diameter 816 mm		wheel diameter 815 mm		wheel diameter 824 mm		wheel diameter 823 mm		wheel diameter 823 mm		wheel diameter 823 mm		wheel diameter 819 mm		wheel diameter 820 mm	
0	FT	30.953	30.944	30.983	30.784	31.099	30.957	30.938	31.076	30.401	30.367	30.830	30.987	30.437	30.717	30.852	30.933
	FH	27.970	27.894	28.141	28.043	27.969	28.187	28.030	28.271	28.245	27.918	28.141	27.982	28.013	27.937	28.333	27.883
	QR	10.208	10.140	10.424	10.457	10.220	10.306	10.279	10.833	10.332	10.445	10.364	10.219	10.421	10.500	10.338	10.396
1426	FT	29.855	28.977	30.283	29.317	30.118	29.383	30.152	29.450	29.796	29.799	30.288	29.483	29.802	29.085	30.267	29.316
	FH	28.010	27.923	28.104	28.108	28.000	28.249	28.095	28.278	28.248	28.284	28.247	28.030	28.997	28.003	30.383	27.919
	QR	9.297	8.226	9.822	8.956	9.344	8.749	9.511	9.072	9.635	9.767	9.773	8.763	9.593	8.883	9.675	8.762
2001	FT	29.056	28.498	29.722	28.878	29.441	28.667	29.629	28.717	29.153	28.101	29.739	28.841	29.066	28.447	29.625	28.777
	FH	27.990	27.880	28.161	28,0,80	29.998	28.248	28.128	28.283	28.290	27.994	28.273	28.022	28.027	28.014	28.362	27.957
	QR	8.404	7.558	9.233	8.637	8.702	7.950	8.873	8.436	9.144	8.141	9.236	8.086	9.038	8.152	9.248	8.373
2575	FT	28.259	27.096	29.333	28.045	28.972	28.385	29.029	28.124	29.053	27.600	29.095	28.505	28.553	27.866	29.205	28.473
	FH	28.009	27.089	28.173	28.020	28.063	28.243	28.090	28.241	28.285	27.963	28.244	28.085	28.030	28.018	28.352	27.968
	QR	7.198	7.024	8.853	8.163	8.123	7.598	8.438	7.791	8.868	7.395	8.559	7.840	8.372	7.340	8.777	7.900

Figure 16. The experimental data of the ALn 501 ‘Minuetto’ MD061.

5.2. *Wheel profile reference dimensions*

According to [18], the wear progress in a wheel profile can be easily represented through three reference dimensions, avoiding a complete detection of the shape: the *flange thickness* (FT), the *flange height* (FH) and the QR dimension, Figure 15. These quantities are defined in the following manner:

- the point P0 on the profile is 70 mm distant from the internal side of the wheel;
- the point P1 is 2 mm above the lowest point V of the flange on the wheel profile;
- the point P2 is 10 mm below P0 on the profile and
- the FT is defined as the distance between P2 and the internal vertical side of the wheel; QR is the horizontal distance between P1 and P0; the FH is the vertical distance between P0 and V.

Because of the way the quotas are defined, they are positive and do not depend on the wheel rolling radius. The values of these parameters are measured periodically in order to decide whether the profile has to be re-turned or not (if it is still possible), considering the maximum or minimum values suggested by the regulation in forces [18]. The check of the reference quotas aims to guarantee mainly the safety against the hunting and the derailment, as well as an acceptable running behaviour. With regard to their physical meaning, both

km	flange dimensions	1 r	1 l	2 r	2 l	3 r	3 l	4 r	4 l	5 r	5 l	6 r	6 l	7 r	7 l	8 r	8 l
		wheel diameter 846 mm		wheel diameter 846 mm		wheel diameter 846 mm		wheel diameter 846 mm		wheel diameter 846 mm		wheel diameter 846 mm		wheel diameter 846 mm		wheel diameter 846 mm	
0	FT	30.919	31.320	30.754	30.825	30.934	30.549	31.083	30.626	31.066	31.038	31.002	30.758	30.687	30.957	30.895	30.709
	FH	28.270	27.826	28.329	27.968	28.137	28.084	28.091	28.084	28.257	27.995	28.295	27.811	28.390	27.651	28.221	27.518
	QR	10.613	10.083	10.716	10.273	10.430	10.006	10.024	10.006	10.511	10.364	10.509	10.408	10.700	10.338	10.335	10.080
1050	FT	30.428	29.918	30.259	29.803	30.390	29.358	30.333	29.513	30.582	29.723	30.367	29.488	30.191	30.580	30.415	29.004
	FH	28.228	27.876	28.325	27.922	28.148	28.006	28.091	28.112	28.262	28.092	28.307	27.884	28.383	27.710	28.245	27.552
	QR	10.134	8.684	10.377	9.267	9.973	8.740	9.615	8.834	9.980	9.083	10.130	8.998	10.202	8.965	9.895	8.370
2253	FT	28.753	28.218	29.117	29.014	28.776	27.530	28.970	28.218	28.687	27.722	29.022	27.512	28.809	27.845	29.141	27.306
	FH	28.304	27.911	28.344	28.054	28.202	28.104	28.085	28.216	28.295	28.099	28.320	27.926	28.382	27.698	28.318	27.632
	QR	8.604	7.209	9.130	8.382	8.294	7.326	8.238	7.343	8.395	7.444	8.793	7.274	8.862	7.065	8.662	7.034
2576	FT	28.142	27.978	29.128	28.867	28.690	27.570	29.122	28.008	28.465	27.621	28.888	27.448	28.482	27.882	28.829	26.971
	FH	28.278	27.883	28.335	28.037	28.213	28.102	28.113	28.171	28.236	28.172	28.341	27.889	28.406	27.792	28.180	27.581
	QR	8.142	7.111	9.032	8.237	8.064	7.246	8.213	7.422	8.058	7.319	8.692	7.284	8.470	7.070	8.181	6.940

Figure 17. The experimental data of the ALn 501 'Minuetto' MD068.

km	flange dimensions	1 r	1 l	2 r	2 l	3 r	3 l	4 r	4 l	5 r	5 l	6 r	6 l	7 r	7 l	8 r	8 l
		wheel diameter 846 mm		wheel diameter 846 mm		wheel diameter 846 mm		wheel diameter 846 mm		wheel diameter 846 mm		wheel diameter 846 mm		wheel diameter 846 mm		wheel diameter 846 mm	
0	FT	30.973	30.778	31.045	30.737	30.894	30.923	30.882	30.809	30.904	30.564	30.899	31.164	30.616	30.976	30.867	30.838
	FH	28.239	27.916	28.032	27.851	28.294	27.947	28.260	27.910	28.196	27.918	28.100	27.931	28.064	28.071	27.958	28.143
	QR	10.447	10.108	10.518	10.274	10.728	10.229	10.782	10.178	10.474	10.483	10.559	10.283	10.441	10.202	10.313	10.321
852	FT	30.917	30.360	30.836	30.311	30.563	30.429	30.824	30.276	30.910	30.092	30.666	30.536	30.317	30.564	30.530	30.141
	FH	28.189	28.043	28.040	27.917	28.332	28.050	28.331	28.008	28.237	27.914	28.170	28.002	28.213	28.126	27.866	28.130
	QR	10.141	9.800	10.256	9.912	10.405	9.865	10.466	9.951	10.284	10.015	10.220	9.812	10.496	9.721	10.147	9.835
1800	FT	29.732	29.221	30.039	29.238	29.880	29.304	30.039	29.273	29.861	28.849	30.221	29.317	29.644	29.682	29.969	28.716
	FH	28.209	28.001	28.009	27.908	28.374	27.995	28.240	28.061	28.285	27.923	28.165	28.014	28.110	28.126	27.975	28.179
	QR	9.206	8.619	9.503	8.765	9.672	8.644	9.831	8.792	9.372	8.856	9.609	8.650	9.334	8.992	9.321	8.341
2802	FT	28.439	28.114	29.278	28.364	28.854	28.568	29.557	27.885	28.527	27.958	29.497	28.178	28.552	28.907	29.100	27.727
	FH	28.165	28.044	28.088	27.897	28.287	28.024	28.293	28.045	28.233	27.883	28.128	27.931	28.072	28.126	27.562	28.201
	QR	7.844	7.348	8.733	7.885	8.762	7.871	9.065	7.486	8.385	7.885	9.009	7.321	8.172	8.224	8.390	7.431
3537	FT	28.160	27.821	29.012	28.121	28.523	28.306	28.998	27.566	28.260	27.643	28.538	27.804	28.054	28.658	28.524	27.244
	FH	28.196	28.021	28.062	27.928	28.320	28.056	28.298	27.996	28.314	28.002	28.229	27.956	28.067	28.130	28.075	28.202
	QR	7.106	7.234	8.460	7.553	8.383	7.608	8.707	7.111	7.809	7.455	8.229	7.176	7.920	7.917	7.851	7.273

Figure 18. The experimental data of the ALn 501 'Minuetto' MD082.

the FT and the FH describe the size of the flange, while the FH is also a measure of the wear on the wheel tread. The QR dimension gives information related to the conicity of the flange.

5.3. *Treatment of the experimental data*

The experimental data used in the model validation are the evolutions of the reference dimensions measured on three different ALn 501 'Minuetto' during the service on the Aosta–Pre Saint Didier railway line. These vehicles are conventionally named MD061, MD068 and MD082 and Figures 16–18 show, respectively, the dimension progress for all the wheels of each vehicle as a function of the travelled mileage (equal to 2500 km for MD061 and MD068; equal to 3500 km for MD082). In the numerical simulations, the distance of 3500 km (km_{tot}) was divided into $N_{step} = 10$ steps, with a resulting km_{step} equal to 350 km, corresponding to a km_{runs} equal to 400 m (Table 4). To make a comparison with the profile arising from the simulations possible, a single wheel profile progress for each vehicle was evaluated taking the average of the values of the quotas on the 16 wheels (the mean results are given in Table 5). The data processing consisted of the following steps:

- scaling of the dimensions to eliminate the initial offsets, imposing the nominal values at the beginning of the mileage, and

- average of each dimension on the 16 wheels of a vehicle, in order to establish a single wheel profile progress to be compared with the numerical results.

The two steps were performed on each 'Minuetto' (MD061, MD068 and MD082) without further averages on the three vehicles, preserving the mean behaviour of each of them and guaranteeing a tolerance zone for a better and more significant experimental data fitting.

5.4. *Progress of the reference dimensions*

This section presents the first results of the validation, showing the comparison between the numerically evaluated progresses of the three dimensions (FT, FH and QR) and the treated experimental data. A certain difference between the numerical results and the experimental data can be observed, probably due to the presence of other wear mechanisms; on average, the wear rate is slightly underestimated. In this regard, the filter has been used to cut the numerical noise only; by way of example, the function of removed material $\bar{\Delta}_{sm}$ (after taking the average on wheels and simulations and before scaling the mileage) is shown in Figure 19 compared with the same function before applying the filter.

The progress of the FT dimension is shown in Figure 20; as it can be seen, the decrease in the quota is almost linear with the travelled mileage except in the first phases, where the profiles of the wheel and the rail are not conformal enough. The FH curve progress is presented in Figure 21, which shows that due to the presence of many sharp curves in the track and the low travelled mileage, the wear is localised mainly on the flange rather than on the tread; thus the FH remains nearly constant.

The comparison between the real QR and the simulated QR is shown in Figure 22: the dimension decreases almost linearly too, leading to an augmentation of the conicity on the flange. Although the simulated mileage is quite short considering the mean travelled distance

Table 4. The values of km_{tot}, km_{step} and km_{runs}.

km_{tot} (km)	km_{step} (km)	km_{runs} (km)
3500	350	0.4

Table 5. Averaging and scaling of the experimental data.

		QR (mm)		FH (mm)		FT (mm)	
Vehicle	km	Mean	Standard deviation	Mean	Standard deviation	Mean	Standard deviation
MD061	0	10.8	0.16	28.0	0.14	32.5	0.23
	1426	9.8	0.48	28.2	0.61	31.5	0.43
	2001	9.1	0.52	28.1	0.51	30.8	0.50
	2575	8.6	0.60	28.0	0.28	30.2	0.63
MD068	0	10.8	0.24	28.0	0.25	32.5	0.20
	1050	10.0	0.65	28.0	0.23	31.8	0.49
	2253	8.5	0.73	28.0	0.23	30.2	0.64
	2576	8.4	0.64	28.0	0.22	32.5	0.65
MD082	0	10.8	0.19	28.0	0.14	32.5	0.15
	852	10.6	0.25	28.0	0.14	32.3	0.26
	1800	9.6	0.44	28.0	0.13	31.3	0.44
	2802	8.7	0.58	28.8	0.18	30.3	0.56
	3537	8.3	0.51	28.1	0.13	30.0	0.50

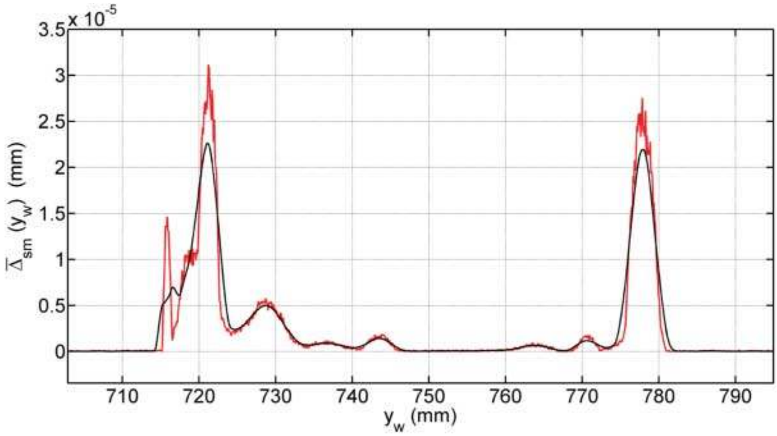

Figure 19. The function of removed material $\bar{\Delta}_{sm}$: before applying the filter (in red) and after applying the filter (in black).

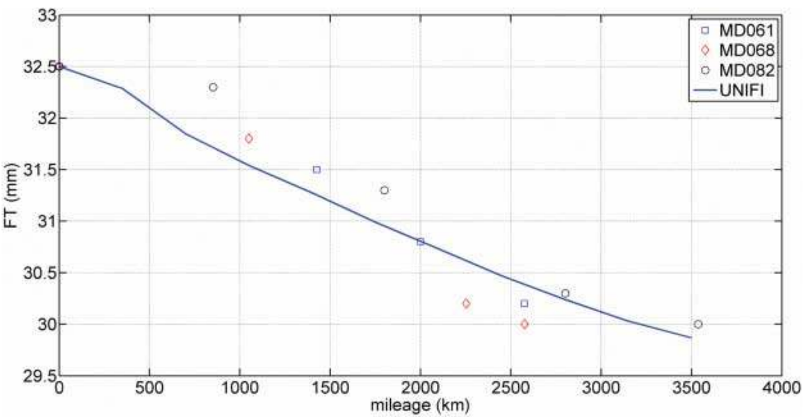

Figure 20. The FT dimension progress.

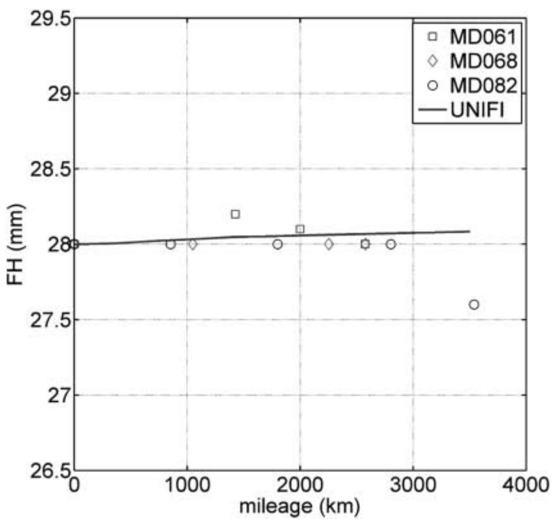

Figure 21. The FH dimension progress.

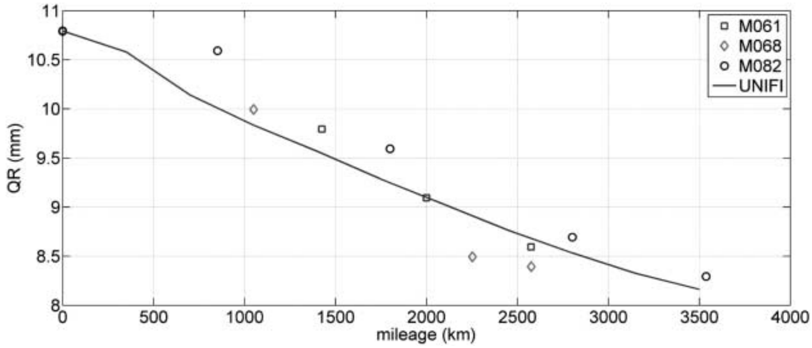

Figure 22. The QR dimension progress.

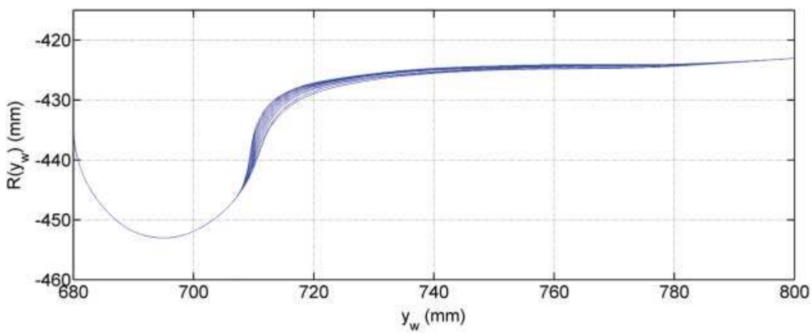

Figure 23. The evolution of the wheel profile.

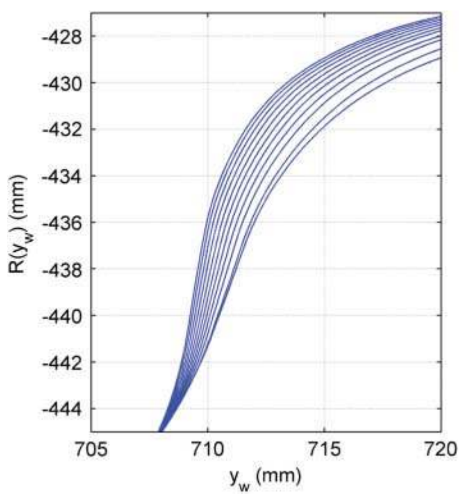

Figure 24. The evolution of the profile in the flange zone.

between two turnings of the wheels in a normal scenario, the variations in the FH and QR dimensions are remarkable and evidence difficulties in terms of wear in travelling on this railway line with this vehicle.

As a conclusion, the comparisons show that the outputs of the wear model are very consistent with the experimental data, both for the flange dimensions (FT, FH) and the QR; therefore, the validation of the model can be considered satisfactory.

5.5. *Progress of the wheel profile*

The numerical evolution of the wheel profile is shown in Figure 23. Due to the low covered mileage and to the sharpness of the track, the wear is mainly localised on the flange rather than on the tread, where it is quite low and implies a slight reduction of the rolling radius.

However, with regard to the flange zone, the wear rate is higher during the initial steps because of the non-conformal contact due to the coupling between the ORE S1002 wheel profile and the UIC60 rail with a inclination of 1:20 rad; then it decreases, becoming more regular and constant in the last phases, when the contact is more and more conformal. The situation is clarified with the zoom on the flange zone, shown in Figure 24: the distance between two consecutive profiles decreases as the wear increases.

6. Conclusions

In this paper, a general model aimed at the wheel wear prediction in railway applications is presented, developed and validated thanks to the collaboration with Trenitalia S.p.A and RFI, which provided the necessary technical and experimental data.

The general structure of the model is made up of two parts which mutually interact during the simulation of a certain prearranged mileage. The first subsystem deals with the vehicle dynamics including both the multibody model of the vehicle implemented in SIMPACK and the global wheel–rail contact model which handles the wheel–rail interaction. The second subsystem is the wear evaluation (made up of the local contact model, the wear model and the wheel profile update), which exploits the outputs of the multibody simulations to evaluate the amount of material to be removed due to wear and to consequently update the wheel profile. The interaction between the two parts occurs in discrete steps; hence, the evolution of the wheel profile is not a continuous time process, but it is described through several intermediate profiles, which are kept constant during the multibody simulations. *The main advantages of the procedure in terms of accuracy and numerical efficiency lie in the employment of the innovative global contact model and in the strategy adopted in updating the wheel profile.*

The whole model has been validated by means of the experimental data relative to a particularly critical scenario in terms of wear in the Italian railways: the ALSTOM Aln 501 'Minuetto' in service on the Aosta–Pre Saint Didier railway line. To reduce the overall computational effort, a statistical equivalent approach to the entire track modelling has been used. As a result, the developed model is able to properly reproduce the evolution of all the three characteristic quotas which describe the wear progress of the wheel profile. Furthermore, the numerical wheel profile evolution highlights the severity of the wear in this particular application, which is highly localised on the wheel flange, according to the frequent maintenance interventions required.

Future developments may concern different aspects. First of all, Trenitalia and RFI will provide further experimental data relative to the Aosta–Pre Saint Didier railway line and other tracks of the Italian Railways; therefore, profile shapes for a further and exhaustive validation will be available. In particular, the experimental data will concern both the advanced wear of the wheels (especially on the tread) and the advanced wear of the rails. As a consequence, the future simulations will be focused on the wheel and rail wear due to longer mileages than on those considered in this work. On the one hand, with regard to the wheel wear, the evaluation will be treated in terms of a mean profile for each wheelset instead of a single profile for the whole vehicle. On the other hand, with regard to the rail wear, two aspects will be investigated: the case of wheel wear using a worn constant rail profile instead of a new profile (as has been done in this work) and the simultaneous evolution of wheel and rail profiles due to wear. Concerning the introduction of other wear mechanisms, phenomena such as fatigue and plastic wear will be introduced in the model.

Finally, further developments will focus on the model optimisation from a numerical point of view: in particular, these improvements will concern the global contact model, the wear model and the general loop.

Acknowledgements

The authors thank Engg. R. Cheli and G. Grande of Trenitalia S.p.A for providing and giving the permission to edit the data relative both to the vehicle ALn 501 Minuetto and to the wheel wear evolution. They also thank the Engg. R. Mele and M. Finocchi of RFI for the data relative to the Aosta–Pre Saint Didier railway line.

References

[1] C. Esveld, *Modern Railway Track*, Delft University of Technology, Delft, Netherlands, 2001.
[2] S. Iwnicki, *Simulation of wheel–rail contact forces*, Fatig. Fract. Eng. Mater. Struct. 26 (2003), pp. 887–900.
[3] F. Braghin, R. Lewis, R.S. Dwyer-Joyce, and S. Bruni, *A mathematical model to predict railway wheel profile evolution due to wear*, Wear 261 (2006), pp. 1253–1264.
[4] T. Telliskivi and U. Olofsson, *Wheel–rail wear simulation*, Wear 257 (2004), pp. 1145–1153.
[5] R. Enblom and M. Berg, *Simulation of railway wheel profile development due to wear: Influence of disk braking and contact environment*, Wear 258 (2005), pp. 1055–1063.
[6] E. Meli, S. Falomi, M. Malvezzi, and A. Rindi, *Determination of wheel–rail contact points with semianalytic methods*, Multibody Syst. Dyn. 20 (2008), pp. 327–358.
[7] M. Malvezzi, E. Meli, J. Auciello, and S. Falomi, *Dynamic simulation of railway vehicles: Wheel–rail contact analysis*, Vehicle Syst. Dyn. 47 (2009), pp. 867–899.
[8] E. Meli, S. Falomi, M. Malvezzi, and M. Rinchi, *Multibody modelling of railway vehicles: Innovative algorithms for the detection of wheel–rail contact points*. ECCOMAS Thematic Conference – Multibody Dynamics 2009, 29th June–2nd July, Warsaw, Poland, 2009.
[9] J.J. Kalker, *Three-dimensional Elastic Bodies in Rolling Contact*, Kluwer Academic Publishers, Dordrecht, Netherlands, 1990.
[10] R.V. Dukkipati and J.R. Amyot, *Computer Aided Simulation in Railway Dynamics*, Dekker, New York, 1988.
[11] S. Iwnicki, *The Manchester Benchmarks for Rail Vehicle Simulators*, Swets & Zeitlinger, Lisse, Netherlands, 1999.
[12] A.A. Shabana and J.R. Sany, *An augmented formulation for mechanical systems with non-generalized coordinates: Application to rigid body contact problems*, Nonlinear Dyn. 24 (2001), pp. 183–204.
[13] A.A. Shabana, K.E. Zaazaa, J.L. Escalona, and J.R. Sany, *Development of elastic force model for wheel/rail contact problems*, J. Sound Vib. 269 (2004), pp. 295–325.
[14] J. Pombo and J. Ambrosio, *Dynamic analysis of a railway vehicle in real operation conditions using a new wheel–rail contact detection model*, Int. J. Veh. Syst. Model. Test. 1 (2005), pp. 79–105.
[15] M. doCarmo, *Differential Geometry of Curves and Surfaces*, Prentice-Hall, Upper Saddle River, NJ, 1976.
[16] F. Cheli and E. Pennestrì, *Cinematica e dinamica dei sistemi multibody*, CEA, Milan, Italy, 2006.
[17] *MATLAB® Official Web Site*. Available at http://www.mathworks.com.
[18] EN 15313 – *Railway applications – In service wheelset operation requirements – In service and off-vehicle wheelset maintenance*. European Committee for standardization, Brussels, April 2010.